




Engineering contact curved interface with high-electronic-state active sites for high-performance potassium-ion batteries

Xuan Li^{a,1}, Yaxin Wang^{a,1}, Junxiong Wu^{a,1}, Lijuan Tong^a, Shuling Wang^b, Xiaoyan Li^{a,2}, Chuanping Li^a, Manxi Wang^a, Manxian Li^a, Weiwei Fan^c, Xiaochuan Chen^a, Qinghua Chen^a, Guoxiu Wang^{d,2} , and Yuming Chen^{a,2}

Edited by Alexis Bell, University of California, Berkeley, CA; received May 4, 2023; accepted October 2, 2023

Potassium-ion batteries (PIBs) have attracted ever-increasing interest due to the abundant potassium resources and low cost, which are considered a sustainable energy storage technology. However, the graphite anodes employed in PIBs suffer from low capacity and sluggish reaction kinetics caused by the large radius of potassium ions. Herein, we report nitrogen-doped, defect-rich hollow carbon nanospheres with contact curved interfaces (CCIs) on carbon nanotubes (CNTs), namely CCI-CNS/CNT, to boost both electron transfer and potassium-ion adsorption. Density functional theory calculations validate that engineering CCIs significantly augments the electronic state near the Fermi level, thus promoting electron transfer. In addition, the CCIs exhibit a pronounced affinity for potassium ions, promoting their adsorption and subsequently benefiting potassium storage. As a result, the rationally designed CCI-CNS/CNT anode shows remarkable cyclic stability and rate capability. This work provides a strategy for enhancing the potassium storage performance of carbonaceous materials through CCI engineering, which can be further extended to other battery systems.

potassium-ion batteries | contact interface | curvature | carbon

The widespread adoption of electric vehicles and smart grids calls for advanced energy storage systems with high energy density, environmental sustainability, low cost, and high-level safety. Although the current electric vehicles are driven by lithium-ion batteries (LIBs), the limited and geographical inhomogeneity of lithium resources retards the worldwide applications of LIBs in large-scale energy storage (1–3). In this regard, developing sustainable batteries with low cost and similar working principles to LIBs is highly demanded. In particular, potassium-ion batteries (PIBs) have gained substantial interest regarding the affluent potassium resources, high energy density, and environmental friendliness, which are the prerequisite requirements for practical applications (4–6). To date, there is still a lack of suitable anode materials for practical PIBs, which deserve more research efforts.

Exploring high-performance anode materials is critical to the success of PIBs. Various anode materials have been extensively studied for PIBs, including carbonaceous materials, alloys, and metal oxides/sulfides/phosphides (7–10). Thereinto, carbonaceous materials have attracted particular interest due to their abundant, adjustable microstructure and chemical stability. Graphite, as a successful anode material in LIBs, can form the LiC_6 intercalation compound with a theoretical capacity of 372 mAh g^{-1} , which triggers great attempts in the PIB system (11). Remarkably, K^+ -ions can intercalate into graphite to form a K-saturated intercalation compound (12), namely KC_8 , which delivers a K storage capacity of 279 mAh g^{-1} . However, the large radius of K^+ -ions hinders their intercalation into graphite layers and leads to notable volume expansion, thus causing severe capacity fading (13). To circumvent the aforementioned issues, porous structures and defects have been designed to improve the K storage performance. Porous nanocarbons are capable of alleviating volume expansion, providing plenty of active sites for K^+ accommodation, and shortening the K^+ /electron diffusion length (14, 15). For example, Cui et al. designed wing-like porous nanocarbons with an ultrahigh surface area of $1,261 \text{ m}^2 \text{ g}^{-1}$, which exhibited a reversible capacity of 347 mAh g^{-1} at 50 mA g^{-1} (16). However, the large surface area will consume excess electrolytes, incurring low Coulombic efficiency (CE) (17). Besides, defect engineering is another efficient method to enlarge the capacity limit of carbonaceous materials. The C–C sp^3 and heteroatom doping defects not only provide efficient K^+ diffusion pathways but promote the absorption of K by adjusting the electronic structure (4). Unfortunately, carbon anodes with massive defects usually exhibit deteriorated electronic conductivity, which is harmful to high-rate performance (18). Therefore, it is still challenging to design carbon architectures with suitable porous structures, proper defects, and tailored electronic properties for realizing high reversible capacity and good rate capability in PIBs.

Significance

Carbonaceous materials, as one of the most promising anode materials for potassium-ion batteries (PIBs), are being widely studied. However, whether and how the contact curved interfaces (CCIs) of carbonaceous materials affect alkali metal-ion storage remains largely unexplored. Herein, we report that CCIs significantly enhance the electronic density of states around the Fermi level of carbonaceous materials and facilitate the adsorption of alkali metal ions using density functional theory calculations. Based on the above rationale, we designed nitrogen-doped, defect-rich hollow carbon nanospheres with abundant CCIs on carbon nanotubes, exhibiting remarkable cyclic stability and rate capability when utilized as an anode material in PIBs. This work provides a perspective on interface engineering to achieve high-performance batteries.

Author contributions: J.W., Xiaoyan Li, and Y.C. designed research; Xuan Li performed research; Y.W., L.T., and S.W. contributed new reagents/analytic tools; Xuan Li, Y.W., J.W., L.T., S.W., Xiaoyan Li, C.L., M.W., M.L., W.F., X.C., Q.C., and Y.C. analyzed data; and Xuan Li, J.W., Xiaoyan Li, G.W., and Y.C. wrote the paper.

The authors declare no competing interest.

This article is a PNAS Direct Submission.

Copyright © 2023 the Author(s). Published by PNAS. This article is distributed under [Creative Commons Attribution-NonCommercial-NoDerivatives License 4.0 \(CC BY-NC-ND\)](https://creativecommons.org/licenses/by-nc-nd/4.0/).

¹Xuan Li, Y.W., and J.W. contributed equally to this work.

²To whom correspondence may be addressed. Email: xiaoyanli1985@126.com, Guoxiu.Wang@uts.edu.au, or yumingc126@126.com.

This article contains supporting information online at <https://www.pnas.org/lookup/suppl/doi:10.1073/pnas.2307477120/-/DCSupplemental>.

Published December 22, 2023.

Recently, curvature effects in carbon nanomaterials have been extensively investigated in electrocatalysts, which could trigger a change in the surface free energy and surface charge density of carbons (19). For example, Li et al. reported that curvature-activated N–C moieties on the hollow carbon surface can serve as the main active sites for oxygen reduction reaction (20). Moreover, Cepitis et al. proposed a realistic in-pore dual-atom metal–nitrogen–carbon site model and utilized density functional theory (DFT) to study the impact of curvature on catalytic activity toward oxygen reduction/oxidation reactions. Their theoretical results confirmed that the surface curvature affects the adsorption energy of each ORR intermediate, hence reducing the overpotential (21). As for energy storage field, Liu et al. reported that a curvature effect of nitrogen doping enlarges the interlayer spacing of nanocarbons and thus enhances their lithium storage performance (22). However, whether and how the contact interface with a curvature of carbonaceous materials affects alkali metal-ion storage remains largely unexplored.

Herein, we first use DFT to study the impact of nitrogen doping and contact curved interface (CCI) on the adsorption of K^+ -ion and electronic structure (Fig. 1). As shown in Fig. 1A, graphene (G), N-doped graphene (N-G), N-doped curved graphene (C_{60} as a typical example), and N-G with a CCI are constructed for comparison. Engineering CCIs in graphene not only favors the adsorption of K (Fig. 1B) but effectively augments the electron population around the Fermi level in comparison with simple surface curvature, hence giving rise to fast electron mobility (Fig. 1C).

In addition, the electron localization function (ELF) results suggest that K primarily interacts electrostatically with different carbon substrates (Fig. 1D). Based on the above rationale, we designed nitrogen-doped, defect-rich hollow carbon nanospheres (NHG-CNSs) with CCIs on carbon nanotubes (CNTs), namely CCI-CNS/CNT. The CCI promotes electron transfer and accommodates massive K^+ -ions, hence improving the potassium storage performance. In addition, the hierarchical hollow structure can suppress the volume expansion upon cycling, maintaining excellent structural stability (Fig. 1E). When used as an anode, the CCI-CNS/CNT exhibits high electrochemical performance, in terms of long cycling life of 5,000 cycles at 4 A g^{-1} and excellent rate performance. This work proposes an approach to improving alkali metal-ion storage performance by CCI engineering.

Results and Discussion

Fig. 2A illustrates the structure of CCI-CNS/CNT and the fast electron/ K^+ transfer in the CCI-CNS/CNT hybrids. The detailed preparation process of CCI-CNS/CNT is displayed in *SI Appendix, Fig. S1*. CNTs are first embedded in polyacrylonitrile/nickel acetate (PAN/Ni(Ac)₂) composite nanofibers via electrospinning, followed by an annealing treatment in an inert atmosphere. The orderly arrangement of CNTs within the electrospun fibers can be attributed to the elongation and surface tension of the fluid during

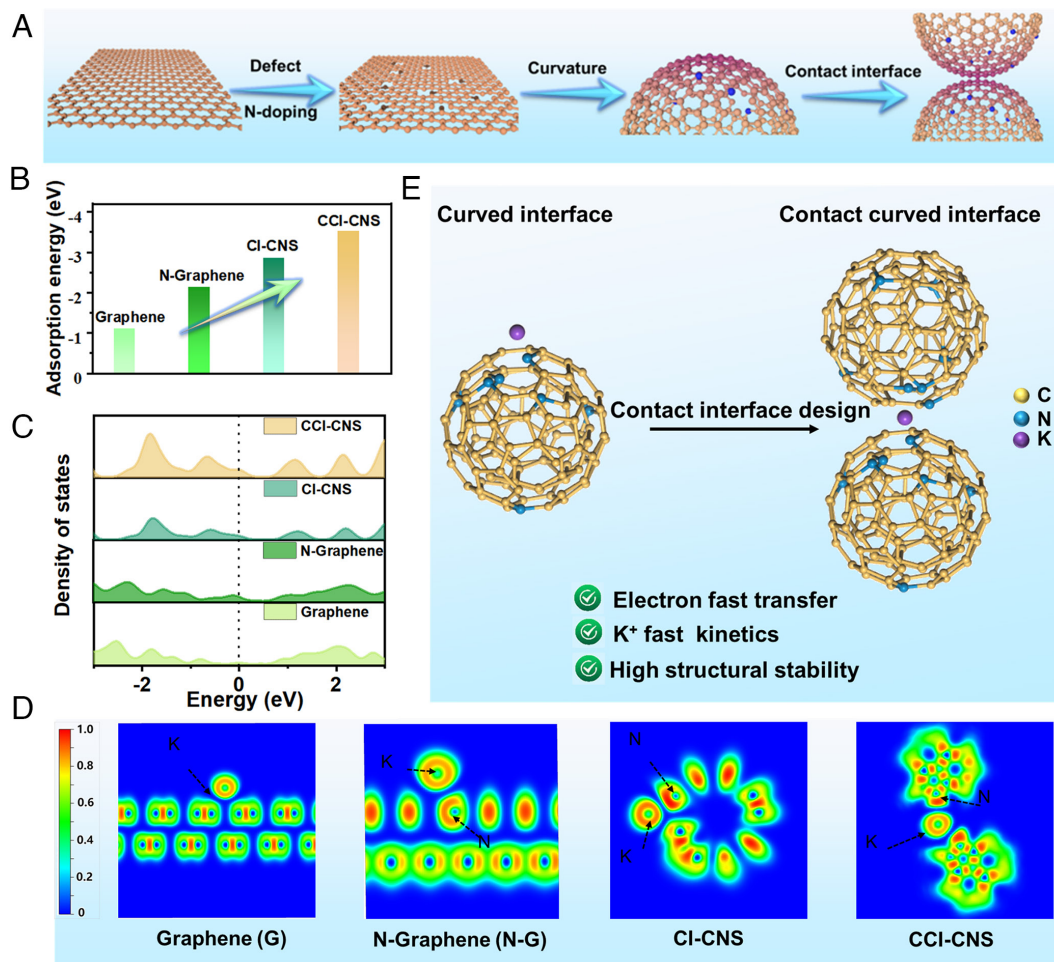


Fig. 1. CCI design correlated with electron transfer and adsorption energy. (A) Illustration of contact interface with curvature. (B) Adsorption energies of a K atom on graphene N-G, CI-CNS, and CCI-CNS. (C) DOS of graphene, N-G, CI-CNS, and CCI-CNS. (D) ELF plots of an isolated K atom on graphene, N-G, CI-CNS, and CCI-CNS. (E) Graphical sketch of the contact curved interface design.

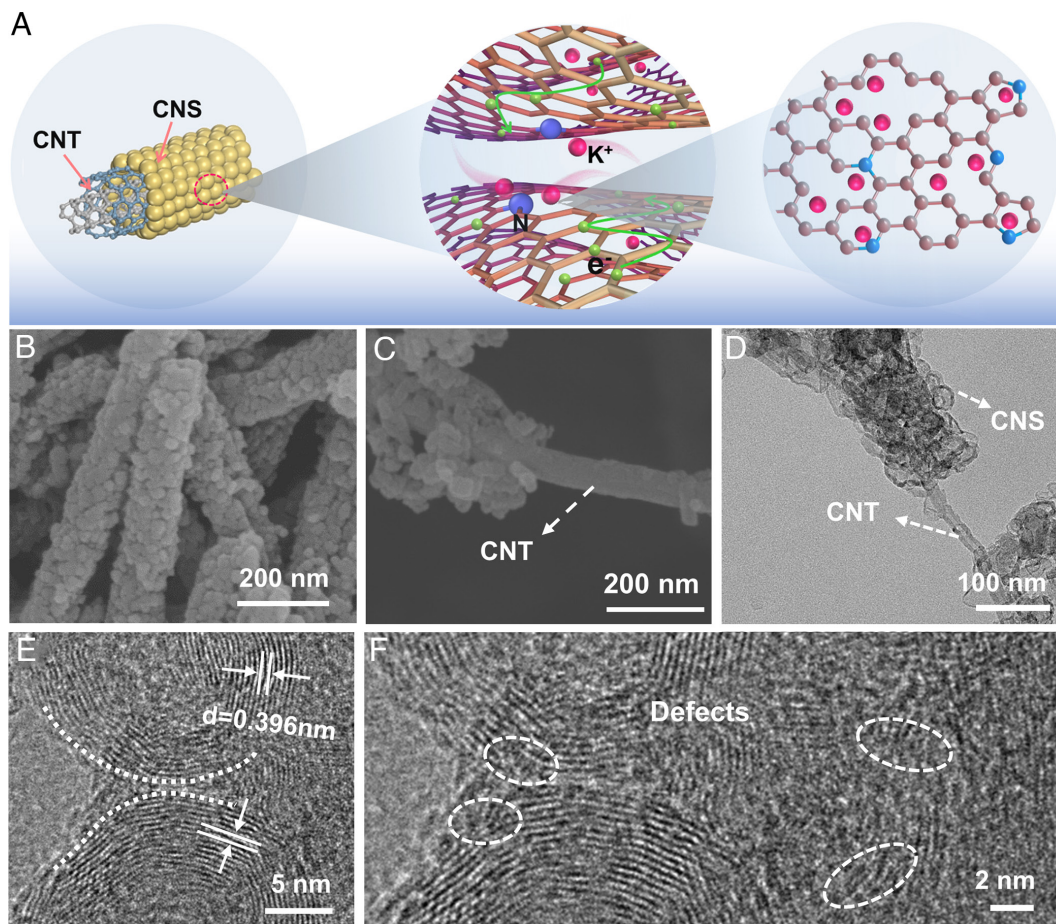


Fig. 2. Morphology and structure of CCI-CNS/CNT. (A) Graphical sketch of the prepared CCI-CNS/CNT and the characteristic of the curved interface. (B and C) scanning electron microscope, (D) transmission electron microscope, and (E and F) high-resolution transmission electron microscope images of CCI-CNS/CNT.

electrospinning (23). During the annealing process, PAN was converted into N-doped amorphous carbon nanofibers (CNFs), while nickel acetate was converted to Ni particles that catalyze the surrounding amorphous carbon into graphitic carbon, yielding the N-doped CNF/CNTs with Ni particles encapsulated in graphitic carbon nanolayers (*SI Appendix, Fig. S2*). After that, a simple HNO_3 -based hydrothermal process was carried out to etch the Ni nanoparticles and selectively decompose the remaining amorphous carbon, thus realizing the assembly of NHG-CNSs on CNTs with abundant CCIs between different CNSs (*SI Appendix, Fig. S3*). Finally, a CO_2 etching treatment was employed to create more defect sites, yielding the N-doped defect-rich graphitic CCI-CNS/CNT sample.

As shown in Fig. 2 B and C, NHG-CNSs are integrated into CNTs to form hierarchical nanofibers with a diameter of $\sim 200 \text{ nm}$. The highly conductive CNTs (with a diameter of $\sim 50 \text{ nm}$) align in the CNFs and serve as internal channels for the rapid diffusion of K^+ and electrons (Fig. 2D and *SI Appendix, Fig. S4*). CCIs are generated between two NHG-CNSs (Fig. 2E), which can offer more interfacial spaces for K^+ storage. Notably, NHG-CNSs show distinct lattice fringes with an extended interlayer spacing of 0.396 nm , which is beneficial for K^+ intercalation/deintercalation. CNS with curved interfaces (CI-CNS) and graphite were also prepared for comparison (*SI Appendix, Figs. S5 and S6*). As shown in Fig. 2F, abundant defects have been successfully introduced into the graphitic carbon matrix. These defects can effectively absorb K^+ ions and facilitate their intercalation into graphite layers through voids between two NHG-CNSs. Therefore, a hierarchical hollow structure with a fast electron transfer route greatly relieves the conflict

between high graphitization degree and the capacity of carbon-based anode materials.

The CCI-CNS/CNT sample was studied using X-ray diffraction (XRD), as shown in Fig. 3A. Two diffraction peaks at 25.8° and 42.9° correspond to the (002) and (100) planes of graphitic carbon (24, 25). Notably, the characteristic peak of the (002) plane is broad due to the existence of defects in the carbon matrix (11). The XRD pattern of the Ni/carbon precursors exhibits four diffraction peaks. In addition to the carbon peak at 25.8° , three prominent peaks located at 44.2° , 51.4° , and 75.8° can be ascribed to the (111), (200), and (220) planes of cubic Ni (*SI Appendix, Fig. S7*) (26, 27). Amorphous carbon is retained in the Ni/carbon hybrid because only a few nanometer-thick amorphous carbon can be converted to graphitic carbon considering the catalytic limit of Ni (28). The Ni particles and amorphous carbon are dissolved and removed during the HNO_3 -based hydrothermal process, leaving pure and highly graphitic CNS/CNT composites, in line with the high-resolution transmission electron microscope results (29). Fig. 3B shows the Raman spectrum of CCI-CNS/CNT with a D-band at $1,351 \text{ cm}^{-1}$ induced by defects, a graphitic G-band at $1,582 \text{ cm}^{-1}$, and a 2D-band at $2,705 \text{ cm}^{-1}$ originating from the second zone-boundary phonons. The I_D/I_G ratio of CCI-CNS/CNT is about 1.41, which is higher than that of CNT (0.94), indicating more defects in the CCI-CNS/CNT carbon matrix (*SI Appendix, Fig. S8*) (30).

The surface area and pore-size distribution were examined to study the porous structure of the CCI-CNS/CNT, as shown in *SI Appendix, Fig. S9*. The N_2 adsorption-desorption isotherm of CCI-CNS/CNT shows a typical IV isotherm, suggesting the existence of mesopores (31). The specific Brunauer–Emmett–Teller

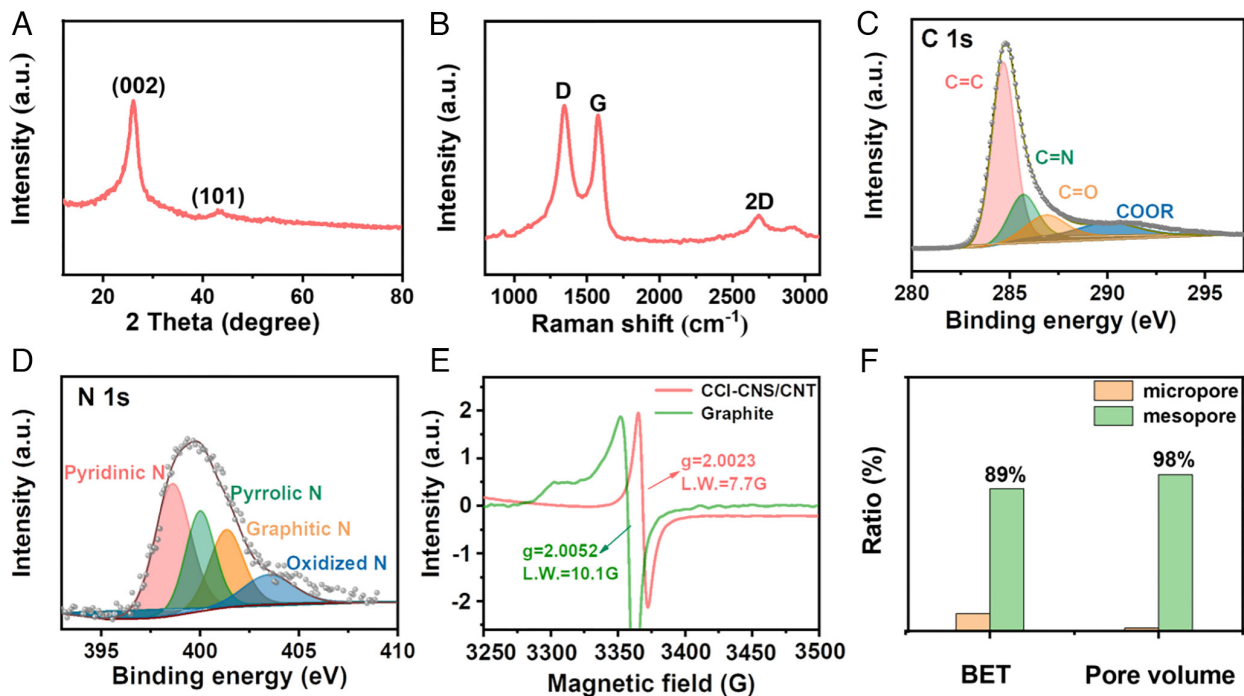


Fig. 3. The characterization of CCI-CNS/CNT. (A) XRD, (B) Raman, (C and D) C 1s, and N 1s XPS spectra of CCI-CNS/CNT. (E) EPR spectra of graphite and CCI-CNS/CNT. (F) The ratio of mesoporous and microporous for Brunauer-Emmett-Teller and pore volume of CCI-CNS/CNT.

surface area of the CCI-CNS/CNT is $\sim 222 \text{ m}^2 \text{ g}^{-1}$. It is obvious that the composite contains hierarchical pores, and the contribution of mesoporous to the total surface area and pore volume is much higher than that of microporous, which is 89% and 98%, respectively (Fig. 3F). The hierarchical pores of the CCI-CNS/CNT composite not only provide affluent sites for accommodating K^+ but also effectively alleviate the volume expansion of highly graphitic CCI-CNS/CNT caused by K^+ intercalation/deintercalation (32, 33).

The elemental mapping analysis of CCI-CNS/CNT demonstrated the uniform distribution of C and N elements in the carbon matrix (SI Appendix, Fig. S10). X-ray photoelectron spectroscopy (XPS) analysis was carried out to study the surface chemistry and chemical bonding state (SI Appendix, Fig. S11). There are three peaks centered at 284.4, 399.5, and 531.9 eV, corresponding to C, N, and O, respectively, indicating the successful doping of N into the CCI-CNS/CNT. For the C 1s spectrum in Fig. 3C, four distinct peaks are recorded at 284.8, 285.7, 286.8, and 290.6 eV, which can be attributed to C=C, C=N, C=O, and -COOR, respectively (5, 34). The N 1s spectrum verifies the existence of pyridinic-N, pyrrolic-N, graphitic-N, and oxidized-N, with binding energies of 398.4, 400.8, 401.6, and 403.2 eV, respectively (Fig. 3D) (35). The N-containing functional groups, especially pyridinic-N and pyrrolic-N can enhance the electronic conductivity of graphitic carbon and induce the capacitive adsorption of K^+ . Importantly, benefiting from the N-doping defect and the CCI engineering, the CCI-CNS/CNT exhibits both a high concentration of N-doped defects and a fast electron transfer route, which are essential for high-performance K storage (36, 37). Based on the elemental analysis, the N content is $\sim 4.1 \text{ wt.}\%$, consistent with the value obtained using XPS, i.e., $\sim 4.5 \text{ wt.}\%$ (SI Appendix, Table S1). The N doping was also investigated using electron paramagnetic resonance (EPR) spectroscopy (Fig. 3E). The graphite shows a distinct Lorentzian line with a center $g = 2.0052$, indicating the presence of mobile electrons from intrinsic defects (38). For comparison, the CCI-CNS/CNT shows a center $g = 2.0023$ and a low line

width, which suggests that unpaired electrons are more localized owing to N-doping defects (39).

We further investigated the relationship between the microstructure and K storage performance of the CCI-CNS/CNT. The CCI-CNS/CNT electrode displays a distinct cathodic peak at 0.6 V vs. K/K^+ during the initial cycle, which can be attributed to the formation of a solid electrolyte interphase (SEI) film on the electrode surface (SI Appendix, Fig. S12) (25, 26). Fig. 4A shows the galvanostatic charge-discharge profile of the CCI-CNS/CNT electrode. The initial discharge capacity in the half-cell is 829.2 mAh g^{-1} at 0.1 A g^{-1} , which could be ascribed to the introduction of defects and mesoporous (4). The charge capacity of the CCI-CNS/CNT is $\sim 370 \text{ mAh g}^{-1}$, corresponding to an initial CE (ICE) of 44%. Furthermore, the CCI-CNS/CNT anode also exhibits remarkable long-term cyclic performance (SI Appendix, Fig. S13 and Fig. 4D). A reversible capacity of 190.8 mAh g^{-1} after 1,000 cycles at 1 A g^{-1} can be retained. At a high current density of 4 A g^{-1} , this anode can still deliver a high capacity of $\sim 100 \text{ mAh g}^{-1}$ after 5,000 cycles with a stable CE of $\sim 100\%$ (Fig. 4D). Without prior electrochemical activation, the CCI-CNS/CNT anode delivers a high initial discharge capacity, which can be attributed to the absence of a stable SEI film on the electrode surface (40). As shown in SI Appendix, Fig. S14, no fragment appears in the CCI-CNS/CNT electrode after 1,000 cycles, illustrating its excellent structural stability upon repeated potassiation/depotassiation processes. Therefore, it is convincing that rich defects and CCIs enable excellent cyclic stability and rate performance.

The rate performance of the CCI-CNS/CNT anode was evaluated at the different current densities ranging from 0.1 to 4 A g^{-1} (Fig. 4B). The CCI-CNS/CNT electrode possesses reversible capacities of 364.0, 326.5, 281.4, 249.3, 211.7, and 185.8 mAh g^{-1} at 0.1, 0.2, 0.5, 1, 2, and 4 A g^{-1} , respectively. Meanwhile, its capacity recovers to 346.2 mAh g^{-1} when the current is shifted back to 0.1 A g^{-1} . It is worth noting that the electrochemical performance of the CCI-CNS/CNT anode surpasses that of other carbonaceous anodes documented in the literature (SI Appendix, Table S2). Electrochemical

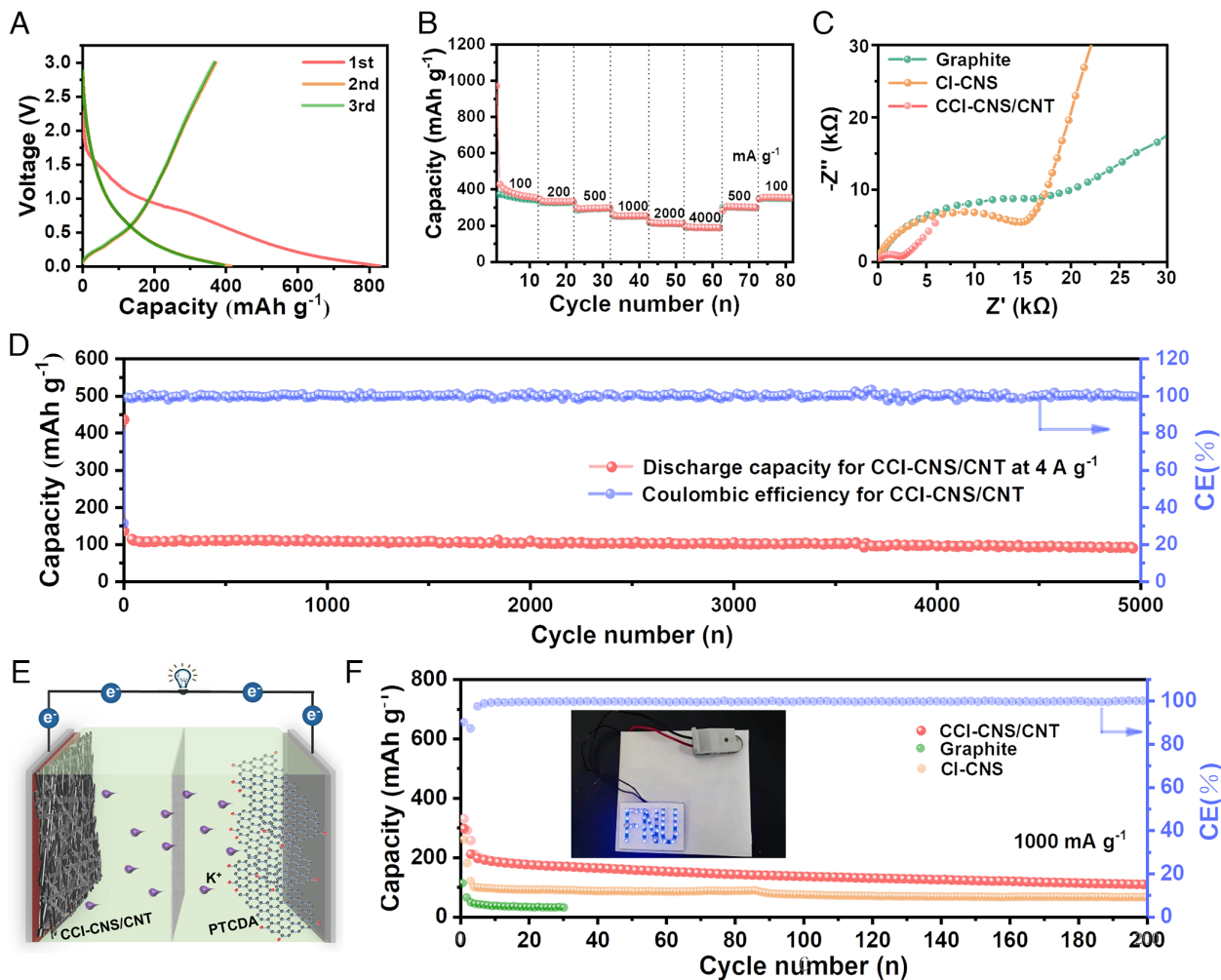


Fig. 4. Electrochemical performances of the CCI-CNS/CNT. (A) Charge–discharge curves at 0.1 A g^{-1} . (B) Rate performance at current densities of $0.1, 0.2, 0.5, 1, 2,$ and 4 A g^{-1} . (C) Nyquist plots of CCI-CNS/CNT, CI-CNS, and graphite electrode. (D) Long-term cyclic performance at 4 A g^{-1} . (E) Schematic illustration of the pPTCDA || CCI-CNS/CNT full-cell. (F) Cyclic performance of the pPTCDA || CCI-CNS/CNT full cells at 1 A g^{-1} (after three activation cycles at 0.1 A g^{-1}) and the *Inset* image shows the full cell can steadily power an LED array.

impedance spectroscopy (EIS) and galvanostatic intermittent titration technique (GITT) were further tested to compare the electrochemical behavior of CCI-CNS/CNT, CI-CNS, and graphite electrodes (Fig. 4C). The CCI-CNS/CNT shows a much smaller charge-transfer resistance (R_{ct}) of $\sim 3,242 \Omega$ compared to that of CI-CNS and graphite (SI Appendix, Table S3). Moreover, the R_{ct} of the CCI-CNS/CNT electrode further decreased to $2,659 \Omega$ after 10 cycles, suggesting a stable structure and efficient ion diffusion in the CCI-CNS/CNT electrode (SI Appendix, Fig. S15 and Table S4) (15). In addition, the CCI-CNS/CNT displays a higher diffusion coefficient (D_{K^+}) than CI-CNS during the discharge process (SI Appendix, Fig. S16), indicating that the CCI-CNS/CNT exhibits better reaction kinetics (34, 41). We also carried out CV tests to study the electrochemical kinetics of the CCI-CNS/CNT (SI Appendix, Fig. S17). The capacitive contribution of the CCI-CNS/CNT was examined by the power-law relationship of the current (i) and scan rate (v): $i = av^b$. The CCI-CNS/CNT electrode exhibits a high b value of 0.86 and 0.95 for cathodic and anodic peaks, respectively, indicating that the storage behavior for the CCI-CNS/CNT electrode is mainly contributed by a capacitive-controlled process. The capacitive contribution ratio of CCI-CNS/CNT electrode can be as high as 73% at the scan rate of 0.6 mV s^{-1} , which further demonstrates that the defects and mesopores facilitate the potassium-ion storage in the reversible adsorption/desorption process (42, 43).

To demonstrate the potential of CCI-CNS/CNT material, PIB full cells were assembled using the prepotassiated perylene tetracarboxylic dianhydride (pPTCDA) as the cathode (Fig. 4E). The pPTCDA cathodes were prepared by electrochemically discharging the PTCDA electrodes to 1.5 V vs. K/K^+ in a half cell, which had a potassium storage capacity of 118 mAh g^{-1} (SI Appendix, Fig. S18) (44). The assembled pPTCDA || CCI-CNS/CNT full cell also exhibits excellent rate and cyclic performance with a high capacity of 110.5 mAh g^{-1} after 200 cycles at 1 A g^{-1} (Fig. 4F and SI Appendix, Fig. S19). Moreover, pPTCDA || CCI-CNS/CNT full cells with higher CCI-CNS/CNT mass loadings (~ 2 and 3 mg cm^{-2}) display almost identical reversible capacities of 130 to 135 mAh g^{-1} after 100 cycles at 1 A g^{-1} , indicating significant potential for practical applications (SI Appendix, Fig. S20). As shown in the *Inset* of Fig. 4F, the assembled full cell can steadily power a 3.0 V LED array.

Since the CCI-CNS/CNT comprises abundant active sites and long graphitic domains, we further studied the detailed K-ion storage mechanism. First, the in situ Raman spectroscopy was carried out to investigate the potassiation/depotassiation process of the CCI-CNS/CNT anode. As displayed in Fig. 5A, the Raman spectrum of pristine CCI-CNS/CNT has characteristic broad D- and G-bands, in agreement with Fig. 3B. During the potassiation process, the D-band becomes broader and mildly moves to a lower

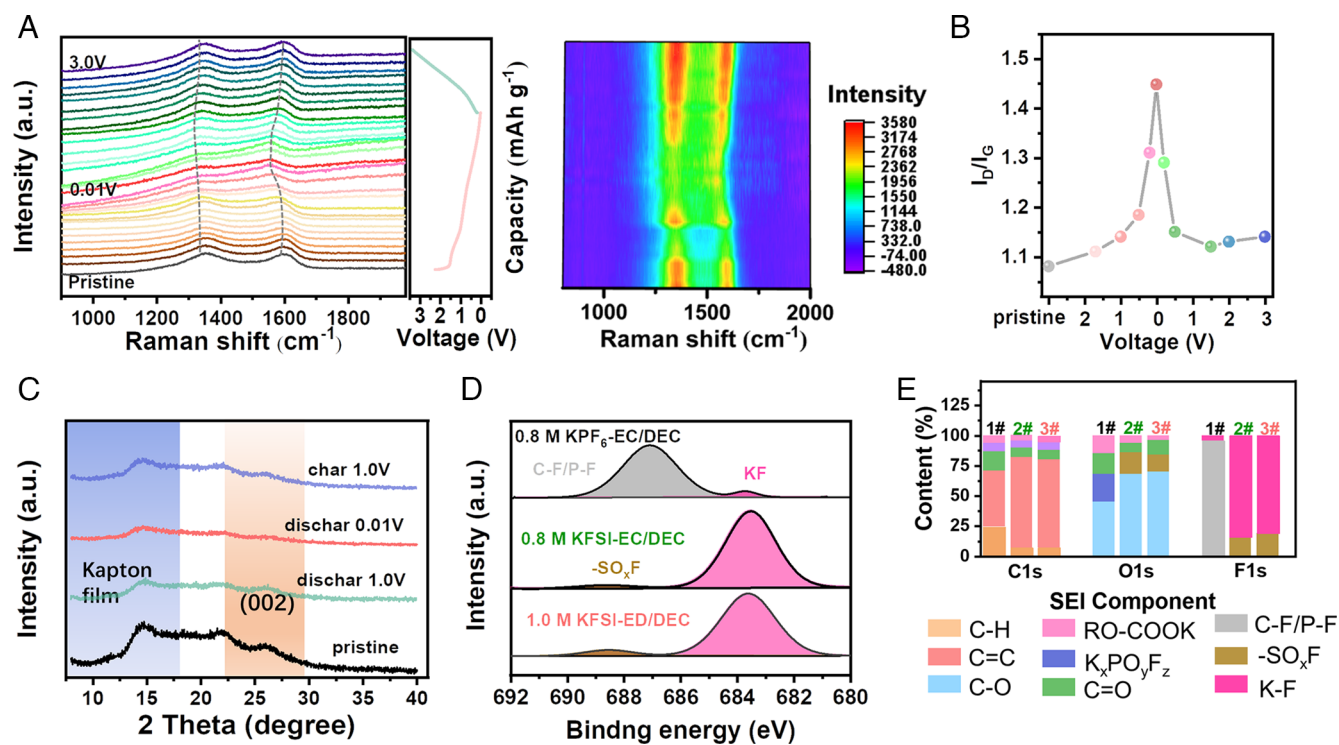


Fig. 5. In situ and ex situ characterizations. (A) In situ Raman spectra and the corresponding contour plot of the CCI-CNS/CNT half cell collected during the first discharge-charge process. (B) The I_D/I_G values as a function of voltage during the first discharge-charge process. (C) Ex situ XRD patterns. (D) Deconvoluted F 1s XPS spectra of the SEIs obtained in different electrolytes. (E) The ratio of SEI components in KFSI-based and KPF₆-based electrolytes.

Raman shift, indicating that K⁺ ions are adsorbed on defect sites (e.g., N-doped defects, carbon vacancies, and micro- and mesopores). The shift of the G-band is clearer, suggesting the K⁺-ion distinctly reacts with sp² carbon. Hence, the storage mode of K⁺ ions is dominated by adsorption at defect sites and further diffusion into the graphite layer, which can be explained by the fast electrochemical kinetic of CCI-CNS/CNT in the discharge process. The I_D/I_G value of CCI-CNS/CNT significantly increased from the original 1.08 to 1.45 when discharging to 0.01 V, and eventually, recovered back to 1.13 for the CCI-CNS/CNT after being charged to 3.0 V (Fig. 5B) (45, 46). The slightly increased I_D/I_G value is mainly caused by the significant internal strain during the potassiation/depotassiation process, which decreases the graphitized degree of carbon, in line with the previous report (47). It is worth noting that the value only increased from 1.08 to 1.13, suggesting the excellent electrochemical reversibility and structural durability of CCI-CNS/CNT (48). As shown in the ex situ XRD in Fig. 5C, there are two distinct diffraction peaks belonging to the Kapton film and the (002) plane of carbon, respectively. The peak intensity of the CCI-CNS/CNT electrode decreases during the discharge process, while it retains when the electrode is recharged to 1.0 V. It is obvious that the K⁺-ions interact with the sp² carbon skeleton, contributing to a change in the intensity of the (002) peak (11). This change is reversible, which is consistent with the in situ Raman result.

We observed that different electrolyte formulations exhibited a distinct electrochemical stability window (ESW) and ICE for the CCI-CNS/CNT electrode. Due to the incomplete dissolution of 1.0 M KPF₆ in the EC/DEC (diethyl carbonate) mixed solvent (SI Appendix, Fig. S21), 0.8 M KPF₆-EC/DEC electrolyte was evaluated. As shown in SI Appendix, Fig. S22, the 0.8 M KPF₆-based electrolyte is prone to be oxidized at ~4.0 V vs. K/K⁺, while potassium bis(fluorosulfonyl)amide (KFSI)-based electrolytes exhibit a higher ESW upper limit of ~4.3 V vs. K/K⁺, proving that KFSI-based electrolytes have better antioxidation capability (49). SI Appendix,

Fig. S23 shows that the 1.0 M KFSI-EC/DEC electrolyte exhibited a slightly higher ionic conductivity of 1.2×10^{-3} S cm⁻¹ compared to the 0.8 M counterpart. Notably, the CCI-CNS/CNT electrodes demonstrated a similar ICE value of approximately 40% in KFSI-EC/DEC electrolytes, which is more than double that obtained in the 0.8 M KPF₆-EC/DEC electrolyte (~19%) (SI Appendix, Figs. S24 and S27B). Among various electrolytes, the CCI-CNS/CNT electrode exhibited highest everisible capacities in 1.0 M KFSI-EC/DEC (SI Appendix, Figs. S25 and S27A). The functional compositions of SEI derived from different electrolyte systems were further studied by ex situ XPS. In the C 1s spectra, RO-COOK, C=O, C-O, C=C, and C-H peaks can be observed both in the KPF₆-based and KFSI-based electrolytes, originating from the decomposition of EC and DEC solvents (50, 51). The O 1s spectra show a K_xPO_yF_z peak and -SO_xF peak in KPF₆-based and KFSI-based electrolytes, respectively (SI Appendix, Fig. S26). Note that in the F 1s spectra, the KPF₆-induced SEI contains C-F/P-F and K-F species, while the SEIs generated in KFSI-based electrolytes include a minor -SO_xF and a dominant K-F component (Fig. 5D) (52). Fig. 5E demonstrates that the KFSI-induced SEI has a much higher KF content than the KPF₆-induced SEI, which could inhibit the decomposition of EC/DEC solvents and the occurrence of side reactions, leading to a substantial improvement in ICE. The SEI components derived from the 0.8 M KFSI-EC/DEC electrolyte resemble those derived from the 1.0 M counterpart, explaining the similar ICE values obtained in the KFSI-based electrolytes. Impressively, we found that using a 1.0 M KFSI-DME electrolyte further improves the ICE to approximately 51% (SI Appendix, Fig. S27 C and D). Therefore, electrolyte engineering represents an effective approach to enhancing ICE.

Furthermore, DFT simulation was performed to provide insight into the influence of curved interface, defect, and N doping on K⁺ storage. Fig. 6 A and B shows the optimized geometric structures of different models containing pure graphene, N-G,

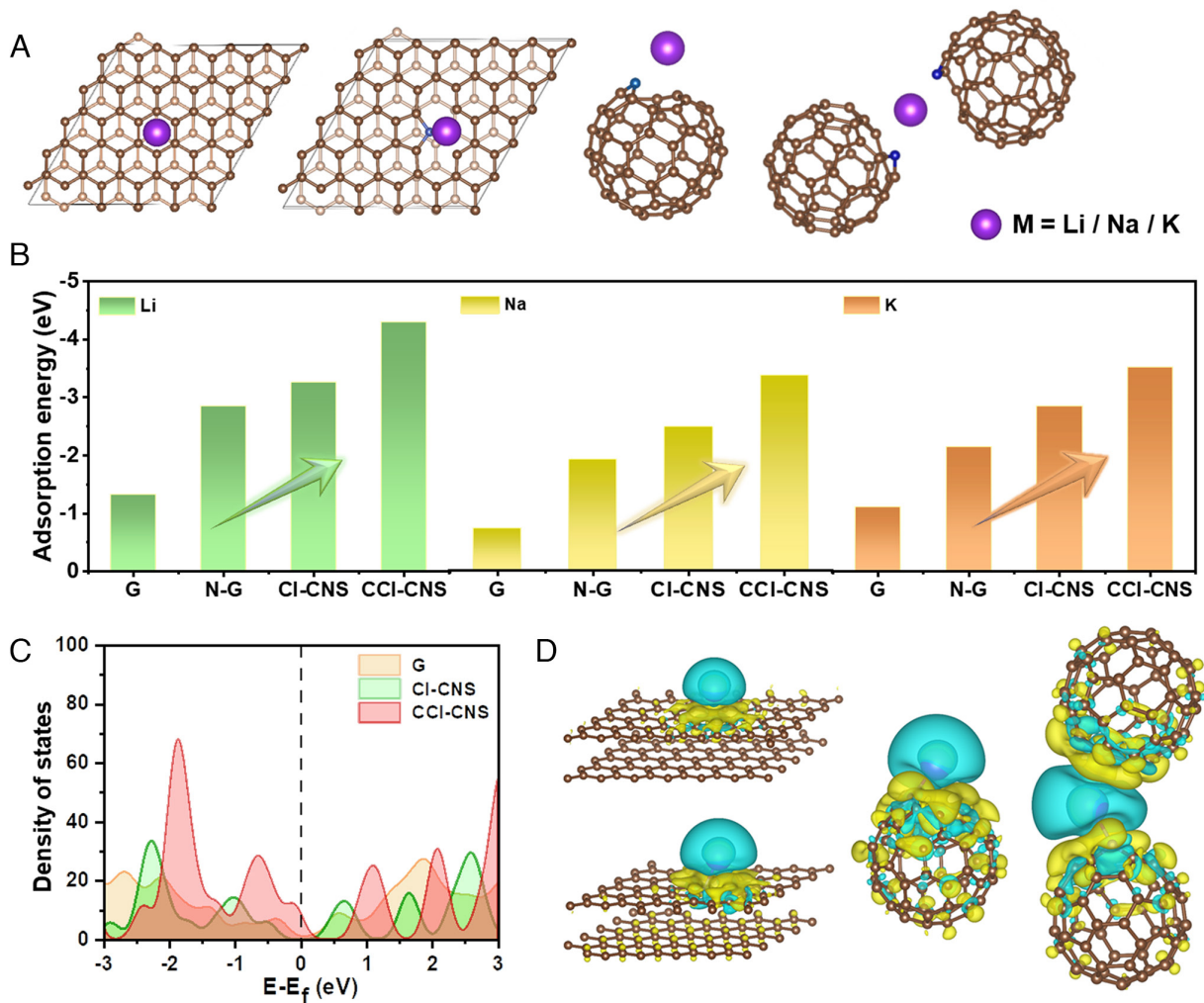


Fig. 6. DFT simulations. (A) The optimized configurations of alkali metal (M) atom adsorbed on pure graphene, N-G, CI-CNS, and CCI-CNS substrates. (B) Adsorption energies of an isolated Li/Na/K on different optimized substrates. (C) DOS of the pure G, N-G, CI-CNS, and CCI-CNS after adsorption of a K atom. (D) Charge density difference plots of an isolated K on pure G (Top Left), N-G (Bottom Left), CI-CNS, and CCI-CNS.

CI-CNS, and CCI-CNS, and the corresponding adsorption energies (E_{ad}) of an alkali metal atom (Li, Na, and K) on the above substrates. Based on the calculation results, the E_{ad} of a K atom on pure graphene, N-G, CI-CNS, and CCI-CNS is calculated to be -1.11 , -2.14 , -2.85 , and -3.52 eV, respectively. The CCI-CNS possesses the most negative E_{ad} (-3.52 eV), indicating that the CCI can strengthen the adsorption behaviors of K. The density of states (DOS) was also performed to figure out the electronic structure of the above-mentioned carbon configurations. As displayed in Fig. 6C, the CCI-CNS exhibits a significant electronic coupling state and the highest electronic concentration around the Fermi level after the absorption of K, thus boosting the storage performance of potassium. We also calculated the charge density differences of different models after K adsorption (Fig. 6D). The charge prefers to aggregate near the joint interface or defect site rather than the surface of the graphite layer. In the CCI-CNS model, most of the charge accumulates at the N-doped site at the curved interface (yellow area) (53). Even without N-doping, the adsorption of K on CCI-CNSs with varying curvatures is more favorable than that on planar graphene and CI-CNSs (SI Appendix, Fig. S28). More importantly, similar results were also verified for lithium and sodium, extending the concept of CCI to other alkali metal-ion batteries (Fig. 6B and SI Appendix, Figs. S29 and S30). To sum up, engineering CCI can enhance the chemical interaction

between the alkali metal ion and carbon network, which is good for alkali metal ion storage in the carbon framework.

Conclusion

In summary, we reported that engineering CCIs enables a favorable enhancement in the electronic DOS around the Fermi level in carbonaceous materials and facilitates their affinity toward alkali metal ions, as supported by DFT calculations. Building upon this understanding, we designed NHG-CNSs with CCIs on CNTs. These distinctive characteristics equip the CCI-CNS/CNT anode with excellent rate performance, an elevated reversible capacity, and a prolonged cycle life (5,000 cycles at 4 A g^{-1}). This work offers an approach for enhancing the potassium storage performance of carbonaceous materials through CCI engineering, which holds promise for broader applications in other battery systems.

Materials and Methods

Preparation of Ni-CNT/CNF. The Ni-CNT/CNF nanofibers were fabricated via electrospinning, followed by a calcination process. To be specific, 1.0 g of PAN and 1.5 g of nickel acetate ($\text{Ni}(\text{Ac})_2 \cdot 4\text{H}_2\text{O}$) were dissolved in 25 mL N, N-dimethylformamide (DMF), namely, solution A. 0.05 g of functionalized CNT was ultrasonically dispersed in 5 mL DMF for 0.5 h to form a solution B. Solution A

and B were then mixed to yield the PAN/Ni(Ac)₂/CNT precursor solution, which was loaded in a syringe for electrospinning. A high voltage of 21 kV and a feed rate of 1.0 mL h⁻¹ were applied. The obtained precursor nanofibers were carbonized at 700 °C for 6 h with a ramping rate of 5 °C min⁻¹ under a flowing N₂ atmosphere in a tube furnace. After cooling down to room temperature, the Ni-CNT/CNF hybrid nanofibers were obtained.

Preparation of CCI-CNS/CNT and CI-CNS. 20 mL of HNO₃ (1 mol L⁻¹) and 0.05 g of Ni-CNT/CNF were added into a Teflon-lined stainless-steel hydrothermal reactor, which was maintained at 160 °C for 10 h in an oven. The obtained composites were rinsed with sufficient ethanol and dried at 80 °C in a vacuum oven. Finally, the CI-CNS/CNT was activated by annealing in a CO₂ flow at 550 °C for 1 h. For the CCI-CNS sample, the same process was applied except that 4 mol L⁻¹ HNO₃ was used during the hydrothermal process.

Materials Characterization. The morphologies and structures of carbon materials were examined using microscope (TEM, FEI Tecnai F30) and field-emission scanning electron microscope (FESEM, Hitachi-8100). X-ray energy dispersive spectroscopy and the elemental analysis (Vario EL cube) were used to investigate the elemental distribution and content. XRD (Bruker D8) was employed to investigate the ordered or disordered structure of carbon materials. The chemical components and defects of carbon materials were investigated by XPS (ESCALAB 250 Xi spectrometer) and EPR spectroscopy (MS 5000X). Nitrogen adsorption/desorption isotherms were performed on Micromeritics ASAP2020. The nonlocal DFT model was performed to calculate the pore size. In situ Raman was performed using a Raman spectroscopy (Raman, DXR2xi) with a 532 nm laser. For ex situ XRD characterization, the cycled electrodes were rinsed with DEC and dried inside the glove box, which were further sealed using a Kapton tape to avoid the reaction with oxygen and water.

Electrochemical Measurement. The electrochemical performance of different samples (e.g., graphite, CI-CNS, and CCI-CNS/CNT) was tested by assembling CR2032 coin cells with potassium metal as the anode in an Ar-filled glove box (H₂O and O₂ < 0.1 ppm). The active material, acetylene black, and carboxymethyl cellulose with a weight ratio of 8:1:1 were mixed to form a uniform slurry, which was spread on the copper foil using a scraper and further dried under vacuum at 80 °C for 10 h. The working electrodes were further cut into disks, and the typical mass loading of active material was about 0.8 to 1.2 mg cm⁻². A glass nanofiber (GF/D, Whatman) was employed as the separator and 0.8 and 1.0 M KFSI or 0.8 M KPF₆ dissolved in ethylene carbonate and DEC (EC: DEC = 1:1 vol%) were used as electrolytes. A controlled amount (60 μL) of electrolyte was added in each cell. The galvanostatic charge/discharge, rate, and GITT tests were performed on the Land battery test system (CT3001A) within the voltage window of 0.01 to 3.00 V. CV and EIS tests ranging from 10⁵ to 0.01 Hz with an amplitude of 5 mV were conducted

on a CHI760E electrochemical workstation. The pPTCDA||CI-CNS/CNT full cells were tested within the potential range of 3.3 to 0.01 V. For full cell assembly, the graphite, CI-CNS, and CCI-CNS/CNT electrodes were precycled for 10 cycles and the PTCDA cathode was prepotassiated at 1.3 V.

DFT Simulations. DFT-based first-principles calculations were performed by using ABINIT codes (54, 55). The exchange-correlation functional was treated by the generalized gradient approximation with the parametrization scheme of Perdew–Burke–Ernzerhof (PBE) (56). The electron–ion interactions were considered by projector-augmented-wave potentials. A cutoff energy of 20 Ha is used and the DFT–D2 approach was applied to take into account the long-range van der Waals interaction (57). A 4 × 4 supercell of graphene was employed and a vacuum layer of 20 Å was used in the z direction to eliminate the interaction between adjacent graphene sheets. The Brillouin zone was sampled using a Γ -centered grid (58). The concentration of N-doping was determined based on the XPS results. During structural relaxation and the static self-consistent-field calculation, a 3 × 3 × 1 K-grid was adopted, whereas a 11 × 11 × 1 K-grid was used for DOS calculations. The force convergence criterium for structural optimization was set to 4 × 10⁻⁴ Ha per bohr.

Data, Materials, and Software Availability. This study does not use any custom code or mathematical algorithm, and code availability is not a mandatory requirement for this work. The data that support this work are available in this paper, including [SI Appendix](#) and main text.

ACKNOWLEDGMENTS. X.L., J.W., and Y.C. acknowledge support from the National Natural Science Foundation of China (No. 22179022, No. 22109023, and No. 22209027), the Industry–University–Research Joint Innovation Project of Fujian Province (No. 2021H6006), the Youth Innovation Fund of Fujian Province (No. 2021J05043 and No.2022J05046), FuXiaQian National Independent Innovation Demonstration Zone Collaborative Innovation Platform Project (2022-P-027), the Award Program for Fujian Minjiang Scholar Professorship, and the Talent Fund Program of Fujian Normal University. S.W. thanks support from the Science and Technology Research Project for the Colleges and Universities in Hebei Province (No. QN2022034).

Author affiliations: ^aCollege of Environmental and Resource Sciences and College of Carbon Neutral Modern Industry, Fujian Normal University, Fuzhou, Fujian 350000, China; ^bHebei International Joint Research Center for Computational Optical Imaging and Intelligent Sensing, School of Mathematics and Physics Science and Engineering, Hebei University of Engineering, Handan, Hebei 056000, China; ^cDepartment of Nuclear Science and Engineering, Massachusetts Institute of Technology, Cambridge, MA 02139; and ^dCenter for Clean Energy Technology, School of Mathematical and Physical Sciences, Faculty of Science, University of Technology Sydney, Sydney, NSW 2007, Australia

1. E. Gabriel *et al.*, Heterostructure engineering in electrode materials for sodium ion batteries: Recent progress and perspectives. *eScience* **3**, 100139 (2023).
2. R. Mo, D. Rooney, K. Sun, H. Y. Yang, 3D nitrogen-doped graphene foam with encapsulated germanium/nitrogen-doped graphene yolk-shell nanoarchitecture for high-performance flexible Li-ion battery. *Nat. Commun.* **8**, 13949 (2017).
3. M. Jiao *et al.*, Recycling spent LiNi_{1-x-y}Mn_xCo_y cathodes to bifunctional NiMnCo catalysts for zinc-air batteries. *Proc. Natl. Acad. Sci. USA* **119**, e2202202119 (2022).
4. Y. Chen *et al.*, Defect-selectivity and "order-in-disorder" engineering in carbon for durable and fast potassium Storage. *Adv. Mater.* **34**, 2108621 (2022).
5. J. Lv *et al.*, Single-crystalline Mn-based oxide as a high-rate and long-life cathode material for potassium-ion battery. *eScience* **3**, 100081 (2023).
6. X. Lian *et al.*, Boosting K⁺ capacitive storage in dual-doped carbon crumples with B-N moiety via a general protic-salt synthetic strategy. *Adv. Funct. Mater.* **32**, 2109969 (2022).
7. J. Zheng *et al.*, Extremely stable antimony–carbon composite anodes for potassium-ion batteries. *Energy Environ. Sci.* **12**, 615–623 (2019).
8. Z. Liu *et al.*, Advances and perspectives on transitional metal layered oxides for potassium-ion battery. *Energy Stor. Mater.* **34**, 211–228 (2021).
9. R. C. Cui, B. Xu, H. J. Dong, C. C. Yang, Q. Jiang, N/O dual-doped environment-friendly hard carbon as advanced anode for potassium-ion batteries. *Adv. Sci.* **7**, 1902547 (2020).
10. H. Wu *et al.*, Multidimensional nanobox structural carbon nanofibers with dual confined effect for boosting storage performance and electrochemical kinetics of alkali metal ion batteries. *Chem. Eng. J.* **428**, 131207 (2022).
11. W. Zhang *et al.*, Graphitic vanocarbon with engineered defects for high-performance potassium-ion battery anodes. *Adv. Funct. Mater.* **29**, 1903641 (2019).
12. Z. Jian, W. Luo, X. Ji, Carbon electrodes for K-ion batteries. *J. Am. Chem. Soc.* **137**, 11566–11569 (2015).
13. L. Fan, R. Ma, Q. Zhang, X. Jia, B. Lu, Graphite anode for a potassium-ion battery with unprecedented performance. *Angew. Chem. Int. Ed.* **58**, 10500–10505 (2019).
14. Y. Qian *et al.*, Understanding mesopore volume-enhanced extra-capacity: Optimizing mesoporous carbon for high-rate and long-life potassium-storage. *Energy Stor. Mater.* **29**, 341–349 (2020).
15. W. Feng *et al.*, Liquid-state templates for constructing B, N, co-doping porous carbons with a boosting of potassium-ion storage performance. *Adv. Energy Mater.* **11**, 2003215 (2021).
16. Y. Cui *et al.*, Bioinspired mineralization under freezing conditions: An approach to fabricate porous carbons with complicated architecture and superior K⁺ storage performance. *ACS Nano* **13**, 11582–11592 (2019).
17. B. Wang *et al.*, An insight into the initial Coulombic efficiency of carbon-based anode materials for potassium-ion batteries. *Chem. Eng. J.* **428**, 131093 (2022).
18. R. Dong *et al.*, Elucidating the mechanism of fast Na storage kinetics in ether electrolytes for hard carbon anodes. *Adv. Mater.* **33**, 2008810 (2021).
19. I. Levchenko *et al.*, Nanoengineered carbon-based interfaces for advanced energy and photonics applications: A recent progress and innovations. *Adv. Mater. Interf.* **10**, 2201739 (2023).
20. C. Li, W. Xu, L. Ye, J. Liu, F. Wang, Hydrothermal-induced formation of well-defined hollow carbons with curvature-activated N–C sites for Zn-air batteries. *Chem. Eur. J.* **27**, 6247–6253 (2021).
21. R. Cepitis, N. Kongi, J. Rossmel, V. Ivanišič, Surface curvature effect on dual-atom site oxygen electrocatalysis. *ACS Energy Lett.* **8**, 1330–1335 (2023).
22. H. Liu *et al.*, Curving effects of concave dodecahedral nanocarbons enable enhanced Li-ion storage. *J. Mater. Chem. A* **6**, 14894–14902 (2018).
23. Y. M. Chen, X. Y. Yu, Z. Li, U. Paik, X. W. Lou, Hierarchical MoS₂ tubular structures internally wired by carbon nanotubes as a highly stable anode material for lithium-ion batteries. *Sci. Adv.* **2**, e1600021 (2016).
24. M. Zhang *et al.*, Hierarchically porous N-doped carbon fibers as a free-standing anode for high-capacity potassium-based dual-ion battery. *Adv. Energy Mater.* **9**, 1901663 (2019).
25. W. Zhang *et al.*, Accordion-Like Carbon with high nitrogen doping for fast and stable K ion storage. *Adv. Energy Mater.* **11**, 2101928 (2021).
26. S. Xu *et al.*, The creation of extra storage capacity in nitrogen-doped porous carbon as high-stable potassium-ion battery anodes. *Carbon* **178**, 256–264 (2021).

27. C. C. Yang, D. M. Zhang, L. Du, Q. Jiang, Hollow Ni-NiO nanoparticles embedded in porous carbon nanosheets as a hybrid anode for sodium-ion batteries with an ultra-long cycle life. *J. Mater. Chem. A* **6**, 12663–12671 (2018).
28. Y. Chen *et al.*, Hollow carbon-nanotube/carbon-nanofiber hybrid anodes for Li-ion batteries. *J. Am. Chem. Soc.* **135**, 16280–16283 (2013).
29. X. Li *et al.*, Functionalized N-doped hollow graphitic carbon-nanotube/carbon-nanosphere composite. *Compos. Commun.* **23**, 100578 (2021).
30. Z. Xu *et al.*, Water chestnut-derived slope-dominated carbon as a high-performance anode for high-Safety potassium-ion batteries. *ACS Appl. Energy Mater.* **3**, 11410–11417 (2020).
31. L. Zhang *et al.*, Boosting fast and stable potassium storage of iron selenide/carbon nanocomposites by electrolyte salt and solvent chemistry. *J. Power Sources* **486**, 229373 (2021).
32. Y. Qi *et al.*, A Fe₃N/carbon composite electrocatalyst for effective polysulfides regulation in room-temperature Na-S batteries. *Nat. Commun.* **12**, 6347 (2021).
33. Z. Xu *et al.*, The role of hydrothermal carbonization in sustainable sodium-ion battery anodes. *Adv. Energy Mater.* **12**, 2200208 (2022).
34. B. Xu *et al.*, Regulating potassium ion receptivity by structure engineering in constructing carbon nano-network with optimized nitrogen species. *Mater. Today Energy* **31**, 101223 (2023).
35. Y. Xu *et al.*, Constructing multichannel carbon fibers as freestanding anodes for potassium-ion battery with high capacity and long cycle life. *Adv. Mater. Interf.* **7**, 1901829 (2020).
36. J. Hu, Y. Xie, M. Yin, Z. Zhang, Nitrogen doping and graphitization tuning coupled hard carbon for superior potassium-ion storage. *J. Energy Chem.* **49**, 327–334 (2020).
37. Y. Chen, X. Shi, B. Lu, J. Zhou, Concave engineering of hollow carbon spheres toward advanced anode material for sodium/potassium-ion batteries. *Adv. Energy Mater.* **12**, 2202851 (2022).
38. B. Wang, L. W. Le Fevre, A. Brookfield, E. J. L. McInnes, R. A. W. Dryfe, Resolution of lithium deposition versus intercalation of graphite anodes in lithium ion batteries: An in situ electron paramagnetic resonance study. *Angew. Chem. Int. Ed.* **60**, 21860–21867 (2021).
39. W. Zhang *et al.*, Direct pyrolysis of supermolecules: An ultrahigh edge-nitrogen doping strategy of carbon anodes for potassium-ion batteries. *Adv. Mater.* **32**, 2000732 (2020).
40. L. Yang *et al.*, Constructing active B-N sites in carbon nanosheets for high-capacity and fast charging toward potassium ion storage. *Small* **19**, 2300440 (2023).
41. B. Wang *et al.*, Amorphous carbon/graphite coupled polyhedral microframe with fast electronic channel and enhanced ion storage for potassium ion batteries. *Energy Stor. Mater.* **38**, 329–337 (2021).
42. X. Shi *et al.*, Highly dispersed cobalt nanoparticles embedded in nitrogen-doped graphitized carbon for fast and durable potassium storage. *Nano-Micro Lett.* **13**, 21 (2020).
43. J. Chen *et al.*, Disordered, large interlayer spacing, and oxygen-rich carbon nanosheets for potassium ion hybrid capacitor. *Adv. Energy Mater.* **9**, 1803894 (2019).
44. L. Fan, R. Ma, J. Wang, H. Yang, B. Lu, An ultrafast and highly stable potassium-organic battery. *Adv. Mater.* **30**, 1805486 (2018).
45. S. Zeng *et al.*, Freestanding CNT-modified graphitic carbon foam as a flexible anode for potassium ion batteries. *J. Mater. Chem. A* **7**, 15774–15781 (2019).
46. H. Tan, X. Du, R. Zhou, Z. Hou, B. Zhang, Rational design of microstructure and interphase enables high-capacity and long-life carbon anodes for potassium ion batteries. *Carbon* **176**, 383–389 (2021).
47. K. Jiang, X. Tan, S. Zhai, K. Cadien, Z. Li, Carbon nanosheets derived from reconstructed lignin for potassium and sodium storage with low voltage hysteresis. *Nano Res.* **14**, 4664–4673 (2021).
48. H. Li *et al.*, Mesoporous N, S-rich carbon hollow nanospheres controllably prepared from poly(2-aminothiazole) with ultrafast and highly durable potassium storage. *Adv. Funct. Mater.* **33**, 2301987 (2023).
49. J. Yu *et al.*, In situ fabricated quasi-solid polymer electrolyte for high-energy-density lithium metal battery capable of subzero operation. *Adv. Energy Mater.* **12**, 2102932 (2022).
50. L. Caracciolo, L. Madec, H. Martinez, XPS analysis of K-based reference compounds to allow reliable studies of solid electrolyte interphase in K-ion batteries. *ACS Appl. Energy Mater.* **4**, 11693–11699 (2021).
51. L. Caracciolo, L. Madec, G. Gachot, H. Martinez, Impact of the salt anion on K metal reactivity in EC/DEC studied using GC and XPS analysis. *ACS Appl. Mater. Interf.* **13**, 57505–57513 (2021).
52. Z. Wu, J. Zou, S. Shabanian, K. Golovin, J. Liu, The roles of electrolyte chemistry in hard carbon anode for potassium-ion batteries. *Chem. Eng. J.* **427**, 130972 (2022).
53. D. Qiu *et al.*, Kinetics enhanced nitrogen-doped hierarchical porous hollow carbon spheres boosting advanced potassium-ion hybrid capacitors. *Adv. Funct. Mater.* **29**, 1903496 (2019).
54. X. Gonze *et al.*, First-principles computation of material properties: The ABINIT software project. *Comput. Mater. Sci.* **25**, 478–492 (2002).
55. X. Gonze, A brief introduction to the ABINIT software package. *Z. Kristallogr. Cryst. Mater.* **220**, 558–562 (2005).
56. J. P. Perdew, K. Burke, M. Ernzerhof, Generalized gradient approximation made simple. *Phys. Rev. Lett.* **77**, 3865–3868 (1996).
57. S. Grimme, Semiempirical GGA-type density functional constructed with a long-range dispersion correction. *J. Comput. Chem.* **27**, 1787–1799 (2006).
58. H. J. Monkhorst, J. D. Pack, Special points for Brillouin-zone integrations. *Phys. Rev. B* **13**, 5188–5192 (1976).